

# Molecular beam/infrared reflection-absorption spectroscopy apparatus for probing heterogeneously catalyzed reactions on functionalized and nanostructured model surfaces

Cite as: Rev. Sci. Instrum. **90**, 053903 (2019); <https://doi.org/10.1063/1.5093487>  
Submitted: 21 February 2019 . Accepted: 06 May 2019 . Published Online: 24 May 2019

Smadar Attia, Evan J. Spadafora, Jens Hartmann, Hans-Joachim Freund , and Swetlana Schauermaun 

## COLLECTIONS

 This paper was selected as an Editor's Pick



View Online



Export Citation



CrossMark

## ARTICLES YOU MAY BE INTERESTED IN

[Ultra-low noise magnetic field for quantum gases](#)

Review of Scientific Instruments **90**, 054708 (2019); <https://doi.org/10.1063/1.5087957>

[Closed-cycle, low-vibration 4 K cryostat for ion traps and other applications](#)

Review of Scientific Instruments **90**, 065104 (2019); <https://doi.org/10.1063/1.5088593>

[High sensitivity microwave spectroscopy in a cryogenic buffer gas cell](#)

Review of Scientific Instruments **90**, 053104 (2019); <https://doi.org/10.1063/1.5091773>

Lock-in Amplifiers  
... and more, from DC to 600 MHz



# Molecular beam/infrared reflection-absorption spectroscopy apparatus for probing heterogeneously catalyzed reactions on functionalized and nanostructured model surfaces

Cite as: Rev. Sci. Instrum. 90, 053903 (2019); doi: 10.1063/1.5093487

Submitted: 21 February 2019 • Accepted: 6 May 2019 •

Published Online: 24 May 2019



View Online



Export Citation



CrossMark

Smadar Attia,<sup>1,2</sup> Evan J. Spadafora,<sup>2</sup> Jens Hartmann,<sup>1</sup> Hans-Joachim Freund,<sup>1</sup>   
and Svetlana Schauer mann<sup>2,a)</sup> 

## AFFILIATIONS

<sup>1</sup>Fritz-Haber-Institut der Max-Planck-Gesellschaft, Faradayweg 4-6, 14195 Berlin, Germany

<sup>2</sup>Institut für Physikalische Chemie, Christian-Albrechts-Universität zu Kiel, Max-Eyth-Straße 2, 24118 Kiel, Germany

<sup>a)</sup> Author to whom correspondence should be addressed: [schauer mann@pctc.uni-kiel.de](mailto:schauer mann@pctc.uni-kiel.de)

## ABSTRACT

A new custom-designed ultrahigh vacuum (UHV) apparatus combining molecular beam techniques and *in situ* surface spectroscopy for reactivity measurements on complex nanostructured model surfaces is described. It has been specifically designed to study the mechanisms, kinetics, and dynamics of heterogeneously catalyzed reactions over well-defined model catalysts consisting of metal nanoparticles supported on thin oxide films epitaxially grown on metal single crystals. The reactivity studies can be performed in a broad pressure range starting from UHV up to the ambient pressure conditions. The UHV system includes (i) a *preparation chamber* providing the experimental techniques required for the preparation and structural characterization of single-crystal based model catalysts such as oxide supported metal particles or ordered oxide surfaces and (ii) the *reaction chamber* containing three molecular beams—two effusive and one supersonic, which are crossed at the same point on the sample surface, infrared reflection-absorption spectroscopy for the detection of surface-adsorbed species, and quadrupole mass spectrometry for gas phase analysis. The supersonic beam is generated in a pulsed supersonic expansion and can be modulated via a variable duty-cycle chopper. The effusive beams are produced by newly developed compact differentially pumped sources based on multichannel glass capillary arrays. Both effusive sources can be modulated by a vacuum-motor driven chopper and are capable of providing high flux and high purity beams. The apparatus contains an ambient pressure cell, which is connected to the preparation chamber via an *in situ* sample transfer system and provides an experimental possibility to study the reactivity of well-defined nanostructured model catalysts in a broad range of pressure conditions—up to ambient pressure—with the gas phase analysis based on gas chromatography. Additionally, a dedicated deposition chamber is connected to the preparation chamber, which is employed for the *in situ* functionalization of model surfaces with large organic molecules serving as promoters or modifiers of chemical reactions. We present a general overview of the apparatus as well as a description of the individual components and their interplay. The results of the test measurements involving the most important components are presented and discussed.

Published under license by AIP Publishing. <https://doi.org/10.1063/1.5093487>

## I. INTRODUCTION

A detailed atomistic-level understanding of heterogeneously catalyzed reactive processes is of crucial importance for the rational design of advanced catalysts with high performance. Specifically,

detailed correlations between the microscopic structure of a catalyst and its catalytic performance in terms of activity and selectivity should be obtained to develop new concepts on purposeful structural modifications for improving catalytic efficiency. In many cases, a catalytic surface should contain a combination of multiple

functionalities to promote several reaction steps in a multistep process.<sup>1</sup> One of the most promising ways to approach this concept is based on the functionalization of catalytic surfaces with organic ligands, e.g., organic adsorbates or covalently bonded functional groups, allowing for a selective promotion of the desired reaction path due to lateral reactant-ligand interactions.<sup>2–12</sup> In such functionalized systems, the role of the ligand can be manifold: it can either impose a geometrical constraint on the surface, thus affecting the interaction of the adsorbates with the underlying metal substrate and/or undergo more specific intermolecular interaction, e.g., by building a 1:1 complex with the reactant, thus affecting its electronic structure or adsorption geometry. A number of successful cases of such ligand-directed heterogeneous catalysis were reported recently, in which the surfaces were functionalized with organic ligands to control either chemo-<sup>13–16</sup> or enantioselectivity.<sup>5,11,17,18</sup>

Despite the impressive progress in this field, the development of practically relevant powdered heterogeneous catalysts is frequently relying on a trial and error method. To develop a more rational approach for the synthesis of new functionalized catalytic materials, the atomistic understanding of mechanisms governing ligand-directed heterogeneous catalysis must be significantly improved. Toward this goal, the model catalysis approach offers a unique opportunity to contribute to a deeper understanding of the ligand/adsorbate interactions both on the single crystalline metal surface and on more practically relevant nanostructured model surfaces. Thus, in our recent mechanistic studies on the partial selective hydrogenation of acrolein toward the unsaturated alcohol propenol over Pd model surfaces, we were able to demonstrate that the surface modification with a dense overlayer of organic ligands, particularly, oxopropyl species, turns the Pd(111) surface 100% selective toward the desired hydrogenation of the C=O bond.<sup>19–22</sup> In contrast, on Pd nanoparticles lacking this ligand-overlayer, only minor amounts of propanal resulting from the undesired hydrogenation of the C=C bond were detected.

Finding detailed structure-reactivity relationships in model studies relies on an experimental possibility to investigate reaction mechanisms and kinetics under well-defined isothermal reaction conditions, which can be realized by employing molecular beam techniques providing constant supply of the reactants. This methodology offers several advantages over the traditional tool for addressing reactivity on surfaces—temperature programmed reaction spectroscopy (TPRS). The most serious limitation of TPRS consists in the fact that the reactants can desorb from the surface prior to undergoing a reaction.<sup>23</sup> This problem is particularly important for the hydrogenation of hydrocarbons as we have recently shown in our studies on butene hydrogenation.<sup>24</sup> Constant supply of the reactant and isothermal reaction conditions allow us to prevent such drawbacks and obtain high hydrogenation rates even under ultrahigh vacuum (UHV) conditions.<sup>24</sup> The other major advantage of using molecular beams consists of the possibility to study transient reaction kinetics upon modulation of one of the reactants on a time scale of several milliseconds. Such transient experiments provide valuable information on the reaction mechanisms and the rate limiting steps, which is difficult to achieve in a steady state mode of operation.

Obtaining further insights into the details of the catalytic processes particularly under the more practically relevant ambient pressure conditions requires detailed reactivity studies on well-defined model catalysts beyond the UHV pressure range. Increasing reactant

fluxes might result in considerable changes in the product distribution, structural changes of the catalytic surface, and the ligand layer. These and other pressure-induced effects need to be understood at the atomistic level and correlated with the details of the catalytic process in the UHV pressure range.

In order to combine the experimental methods capable of addressing the challenges described above, we have specifically designed an apparatus that allows us to prepare and characterize ligand-modified model catalysts under well-controlled UHV conditions and address the mechanisms, kinetics, and dynamic of reactive surface processes in the broad range of pressure conditions—from UHV up to the near ambient pressure.

The specific requirements for this experiment can be summarized as follows:

- (1) *Sample preparation and characterization.* The tools for the preparation and characterization of a variety of model catalysts have to be integrated. Particularly, the ability to deposit several metals to prepare different metal oxides and/or metal nanoparticles as well as the ability to modify the surface by deposition of liquid or solid organic modifiers. A sample transfer from the preparation chamber into the reaction chamber under UHV conditions is essential to correlate the kinetic and dynamic information with the structural features of the catalysts under the same well-defined conditions.
- (2) *Molecular beam source* should allow the fast variation of the reactant fluxes over the largest possible range and on a time scale of several milliseconds in order to enable studies on the transient kinetics and accurate identification of the most relevant reaction steps. The molecular beam must be well-collimated and pulsed with a variable modulation frequency. The pulsed molecular beam must be produced in a way that generates only low intensity vibrations in the UHV chamber since the infrared spectrometer and the mercury cadmium telluride (MCT) detector are highly sensitive to mechanical vibrations. For reactivity and selectivity experiments, which require exposure to several reactants, it is necessary to integrate more than one beam source. The beam must be suitable for using a large variety of gases: both gases with high vapor pressure, such as CO and propylene oxide, and large molecules with low vapor pressures ( $<10^{-2}$  mbar) typical for surface modifiers.
- (3) *Surface species detection.* *In situ* detection and monitoring of different co-adsorbed surface species is key to establishing correlations between the catalytic performance of the surface and its chemical and structural composition. In infrared reflection-absorption spectroscopy (IRAS) studies, both the chemical nature of the adsorbates and their orientation with respect to the surface can be determined. The latter question can be addressed by IRAS based on the metal surface selection rule:<sup>25</sup> the vibrational modes exhibiting dynamic dipole moment parallel to the metal surface will not be visible in IRAS, which in many cases allows to derive the relative orientation of the various bonds with respect to the metal surface. Particularly important is the possibility to investigate the changes of the adsorption geometry with changing environment, such as adsorption of a second reactant (e.g., hydrogen), which might have a strong influence on binding

of the organic molecules—both reactants and modifier-ligand; growing modifier-ligand coverage, etc. The experimental setup should ensure chemical resolution as well as low acquisition time for the chemical identification of the adsorbates and *in situ* monitoring the transformations occurring on the surfaces under the reaction conditions.

- (4) *In situ* calibration techniques for determining the absolute values of beam fluxes and their distribution must include a beam monitor for measuring the absolute reactant flux and the beam profile. It should be possible to place the beam monitor at the very same position of the sample with respect to the molecular beams to perform the calibration and adjustment of the beam position.
- (5) *Gas phase detection in UHV*. The gas phase detection must include an integral measurement of sticking and reaction probabilities. The detector should also provide temporal resolution on the time scale of the reaction or scattering experiments typically from the microsecond to the second range.
- (6) *Gas phase detection under ambient pressure conditions*. To study the catalytic performance under the ambient pressure conditions, a dedicated ambient pressure cell (APC) should be implemented, which is separated from the preparation and measurement UHV chambers and can be run as an independent UHV system. The gas phase detection in APC requires gas phase detection methods compatible with ambient pressure conditions. Gas chromatographic detection is the methods of choice allowing us to monitor the reactants and reaction products as well as distinguish between molecules with identical masses (e.g., regio- or enantiomers), which are

normally difficult to differentiate. The transfer system should enable *in situ* transfer of the samples prepared under UHV conditions from the preparation chamber to the APC without breaking vacuum to avoid exposure to air that might destroy or change the catalyst's surface.

In this manuscript, we describe a compact UHV apparatus that combines molecular beam techniques, *in situ* surface spectroscopy, an ambient pressure cell, a chamber for the deposition of liquid and solid organic compounds, and a portable transfer system. The described setup allows us to study surface reactions on a broad range of ligand-functionalized and nanostructured model catalytic systems prepared *in situ* under UHV conditions. We present the detailed arrangement of this multimolecular beam/surface spectroscopy apparatus.

To test the performance of the new apparatus on an already studied metal-ligand system, the adsorption behavior of one of the most efficient and well-studied chiral modifiers,<sup>11</sup> (R)-(+)-1-(1-naphthylethylamine) (NEA) adsorbed on Pt(111) was investigated. As a second test system, acetophenone adsorption on Pt(111) was studied in a broad range of temperature conditions. We provide a discussion on the major observations obtained for both adsorption systems.

## II. SYSTEM DESIGN

### A. Overview

The key components of the new setup are schematically displayed in Fig. 1. The experimental setup operates under UHV

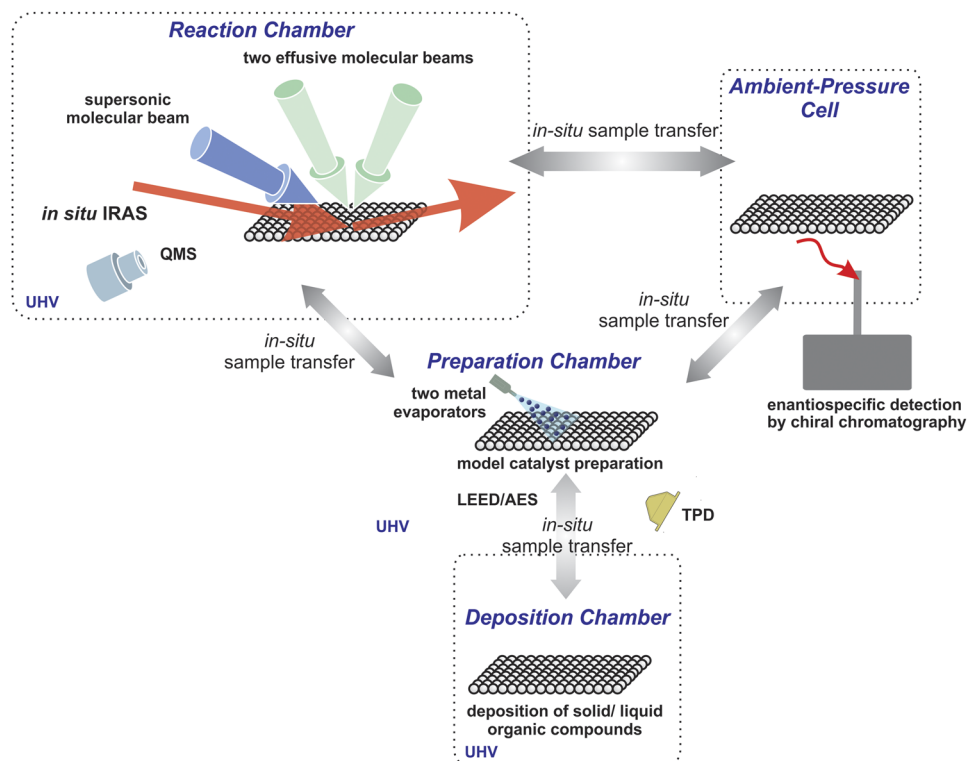


**FIG. 1.** Schematic drawing of the main components of the experimental setup. The apparatus consists of a preparation and reaction chamber, with the latter being equipped with two effusive and one supersonic molecular beams, IRAS, QMS, as well as an APC equipped with a GC for the gas phase detection of reaction products under ambient pressure conditions. The preparation chamber contains LEED/AES, two metal evaporators, TPD setup, sputter gun, and gas dosers. The sample can be transferred *in situ* between all compartments of the apparatus.

conditions and consists of a preparation chamber, a reaction chamber, and an ambient-pressure cell. The chambers are interconnected, and the sample can be transferred *in situ* between the individual chambers through a dedicated transfer setup. The preparation chamber, the reaction chamber, and the ambient pressure cell are designed as three independent UHV systems. The division of the apparatus into the three separate UHV systems was necessary because of the complexity of the preparation procedures of supported model systems, requiring different preparation and characterization techniques, as well as due to spatial limitations resulting from the necessity to simultaneously cross three molecular beams and an infrared beam on the sample surface.

The *preparation chamber* enables the preparation and characterization of different types of catalytic surfaces by means of standard surface science tools ranging from single crystals to more complex nanostructured systems consisting of metallic nanoparticles supported on well-defined single crystalline thin oxide films epitaxially grown on single crystalline metal supports.<sup>26</sup> For the latter surfaces, the size and the density of the metallic nanoparticles can be varied in a broad range by varying the preparation conditions, such as the metal flux, the deposition time, and temperature as well as a number of surface defects serving as nucleation centers for the growth of metallic nanoparticles. The quality and the structural properties of the prepared surfaces can be characterized by standard surface science techniques available in the preparation chamber, which include Low Energy Electron Diffraction (LEED), Auger Electron Spectroscopy (AES), and Temperature Programmed Desorption (TPD). Additionally, the structural and adsorption properties of the model systems can be addressed by performing IR spectroscopy of small adsorbed molecules, such as CO. For this purpose, the sample should be transferred to the *reaction chamber* containing an IR spectrometer as described in the following.

The preparation chamber is connected to a small dedicated *deposition chamber*, in which liquid or solid organic compounds can be deposited by physical vapor deposition onto the model catalyst surface. This procedure allows us to tune the coverage and the distribution of the ligands and by this possibly affect the formation of the intermolecular assemblies on the surface by systematically varying the deposition parameter such as the molecular flux and deposition temperature.

The *reaction chamber* contains three molecular beams (two effusive and one supersonic molecular beam) and *in situ* IRAS. The design of the apparatus allows us to study the reaction mechanisms, kinetics, and dynamics of surface reactions on complex nanostructured model catalysts under UHV conditions. The evolution of the reaction products in the gas phase is monitored by a differentially pumped quadrupole mass spectrometer (QMS), while simultaneous *in situ* monitoring of adsorbed surface species (reactants, ligand modifiers, reaction intermediates, and products) evolving under the reaction conditions can be performed by means of vacuum Fourier transform IRAS (FT-IRAS). Complementary, an APC (Ambient Pressure Cell) is connected to the UHV chamber, providing an experimental possibility to carry out the reactivity studies on the same type of well-defined model surface under ambient pressure conditions by performing gas phase detection via sensitive gas chromatography (GC). Sample transfer in between the different chambers is realized by a combination of two magnetic transfer rods and two manipulators.

Figures 2 and 3(a) show the side and top view drawings of the apparatus. For a better visibility, these figures represent cross sections through different planes of the apparatus, in which only part of the apparatus is visualized. The components described in this chapter are labeled in numerical order, and the corresponding numbers appear complementary in Figs. 2 and 3(a) for a better representation.

Both side view and top view drawings of the apparatus include the preparation [(1) in Figs. 2 and 3(a)] and the reaction [(2) in Figs. 2 and 3(a)] chambers. The chambers are independent UHV systems separated by a gate valve [(3) in Figs. 2 and 3(a), VAT, 10836-CE01] and are pumped by a 560 l/s turbo molecular pump [TMP, Fig. 2 (4), Leybold, Turbovac 600 C] each. The pumps are equipped with magnetic suspension, which reduces vibrations that might potentially interfere with the IR experiments. The typical base pressures in both chambers are  $2 \times 10^{-10}$  mbar. Two manipulators [preparation chamber—manipulator I, Fig. 2 (5), VAB, PM 12-600 and reaction chamber—manipulator II, Fig. 2 (6), VAB, PM 12-200 SZ2] with one rotational and three translational degrees of freedom are placed in the center of each chamber. The manipulator of the preparation chamber has a travel length of 600 mm [manipulator I, Fig. 2 (5)], while the manipulator of the reaction chamber [manipulator II, Fig. 2 (6)] has a travel length of 200 mm and it is equipped with a translational stepper motor for the manipulation of the sample along the z-axis. The combination of both manipulators and the magnetic translational rod [(7) in Figs. 2 and 3(a), VAB, MDS 40-1200] is employed for the sample transfer between the preparation and reaction chambers. The travel length of manipulator I [Fig. 2 (5)] allows the transfer of the sample to the deposition chamber for the deposition of organic compounds in the liquid and solid phases [Fig. 2 (8)]. Details on the setup of the deposition chamber will be given in Sec. II B.

## B. Sample preparation chamber and chamber for the deposition of organic molecules

The assembly of the preparation chamber [Fig. 2 (1)] is divided into two parts. The upper part of the chamber contains all the standard facilities for the preparation of complex nanostructured model catalysts including an ion gun (not shown, SPECS, IQE 11/35), gas doser [Fig. 3(a) (10)], two metal evaporators [Fig. 3(a) (11) and (12), Omicron, EFM3-EVC 300] and quartz crystal microbalance (QCM) for the calibration of the metal fluxes [(13) in Figs. 2 and 3(a), tectra, QMB-im-mod]. The lower part of the preparation chamber contains the tools for the structural characterization of the model catalysts including LEED/AES [(14) in Figs. 2 and 3(a), SPECS, ErLEED 150 4-grids] and QMS [Fig. 3 (15), Hiden, Hal/3F 301 PIC system type 553201]. The preparation chamber is connected to a deposition chamber [Fig. 2 (8)], which is separated by a shutter operated with a rotary motion feedthrough [Fig. 3 (16), MDC, BRM-133] and pumped with 65 l/s TMP (not shown, Leybold, TURBOVAC SL 80). The deposition chamber contains a low temperature effusion cell [Fig. 2 (9), MBE components, NTEZ 40-2-16-S-SF] for the deposition of solid organic compounds, and a gas doser for the deposition of liquid organic compounds (not shown). The preparation chamber is equipped with an additional transfer rod [magnetic transfer rod—Fig. 3(a) (17), VAB, MDS 40-700] which allows the transfer of the sample to the APC [Fig. 3(a) (18)]. The APC is separated

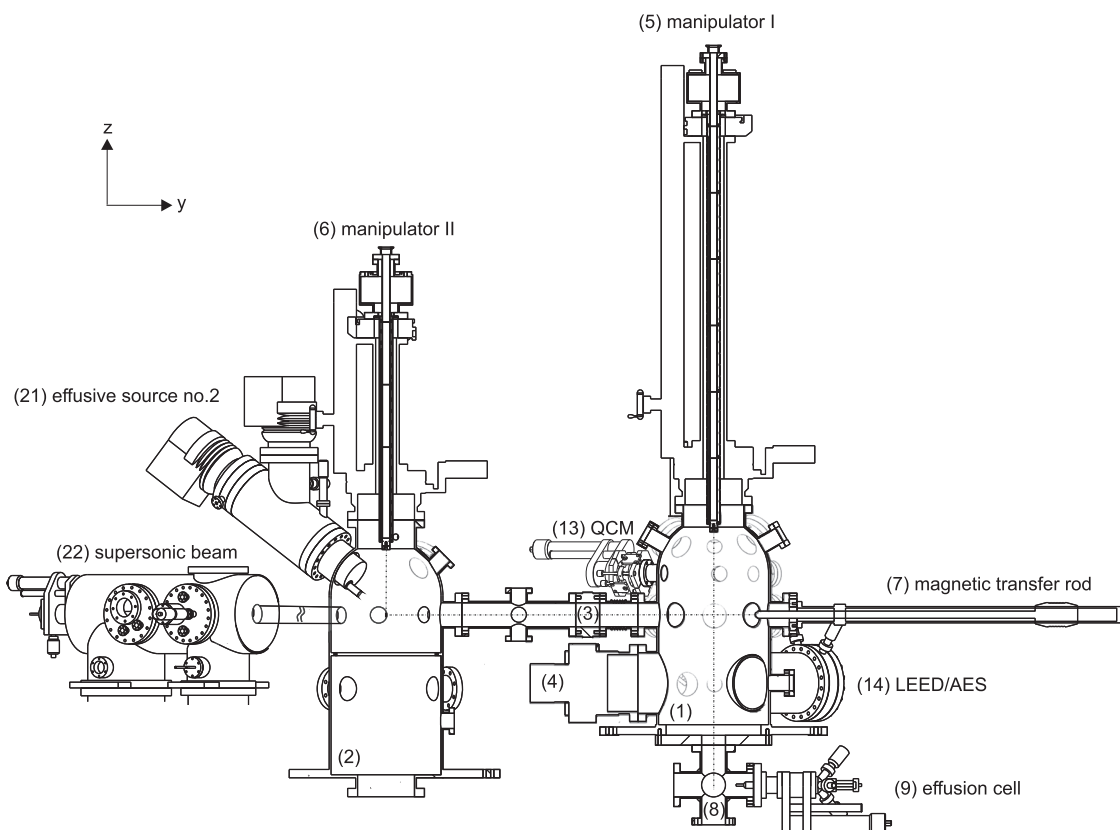


**FIG. 2.** Side view of the experimental setup. A cut-out through the plane of the transfer rod and the manipulators is shown to visualize only the back half of the chambers. The labeled components are (1) preparation chamber, (2) reaction chamber, (3) gate valve, (4) turbomolecular pump of the preparation chamber, (5) sample manipulator I, (6) sample manipulator II, (7) magnetic transfer rod, (8) deposition chamber, (9) effusion cell for the deposition of organic molecules, (13) quartz crystal microbalance (QCM), (14) LEED/AES (21) effusive source no. 2, and (22) supersonic source.

from the preparation chamber by a gate valve [Fig. 3(a) (19), VAT, 10836-CE01] and pumped via a pumping station (not shown, Pfeiffer, HiCube 300H Eco). The details on the setup of the APC are given in Sec. II E.

During the preparation of model catalysts, it is important to reduce the background pressure rise upon dosing of gases. Therefore, a gas doser [Fig. 3(a) (10)] was implemented in the preparation chamber, which is equipped with a manually operated leak valve (VAT, 59024-GE01) and a linear translator (linear travel 101.6 mm, MDC, E-LMT-154, no. 665511). During the gas dosing, the gas phase is monitored by QMS. The distance between the gas doser and the sample can be adjusted from 7 to 60 mm.

For the preparation of complex model catalysts under UHV conditions, two different metals can be deposited onto the sample surface by physical vapor deposition employing two individual electron beam evaporators [Fig. 3(a) (11) and (12)]. To avoid undesirable damage of the samples by ions produced in the electron beam evaporator source, a retarding voltage equal to the acceleration potential of the evaporator is applied (typically 800 V) to the sample during preparation to decelerate those ions. The evaporator fluxes are calibrated using a QCM [(13) in Figs. 2 and 3(a)]. An ion gun and a LEED/AES [(14) in Figs. 2 and 3(a)] are used for sample cleaning

and characterization of the single crystal and the crystallinity of the model oxide films.

Temperature-programmed desorption can be performed in the preparation chamber by means of a QMS equipped with a gold-plated aperture [Fig. 3 (15)]. A proportional integral derivative (PID) based temperature ramp generator (Eurotherm, 2148) allows heating rates of up to 10 K/s.

### C. Reaction chamber

After preparation, the sample is transferred *in situ* to the reaction chamber without breaking ultra-high vacuum. The reaction chamber has an inner diameter of 300 mm and is designed for simultaneous IRAS experiments, reactivity, and sticking probability measurements. Figure 4 shows a schematic representation of the experimental arrangement of the reaction chamber. The exact incidence and detection angles of the main compartments are given in the inset of Fig. 4.

A drawing of the reaction chamber is shown in Fig. 5. This chamber includes two high-flux effusive [Fig. 5 (1) and (2), see also Fig. 3(a) (20) and (21)] and one supersonic [Fig. 5 (3), see also (22) in Figs. 2 and 3(a)] molecular beams. Gas phase detection is performed by means of highly sensitive triple-filter QMS [Fig. 5 (4),

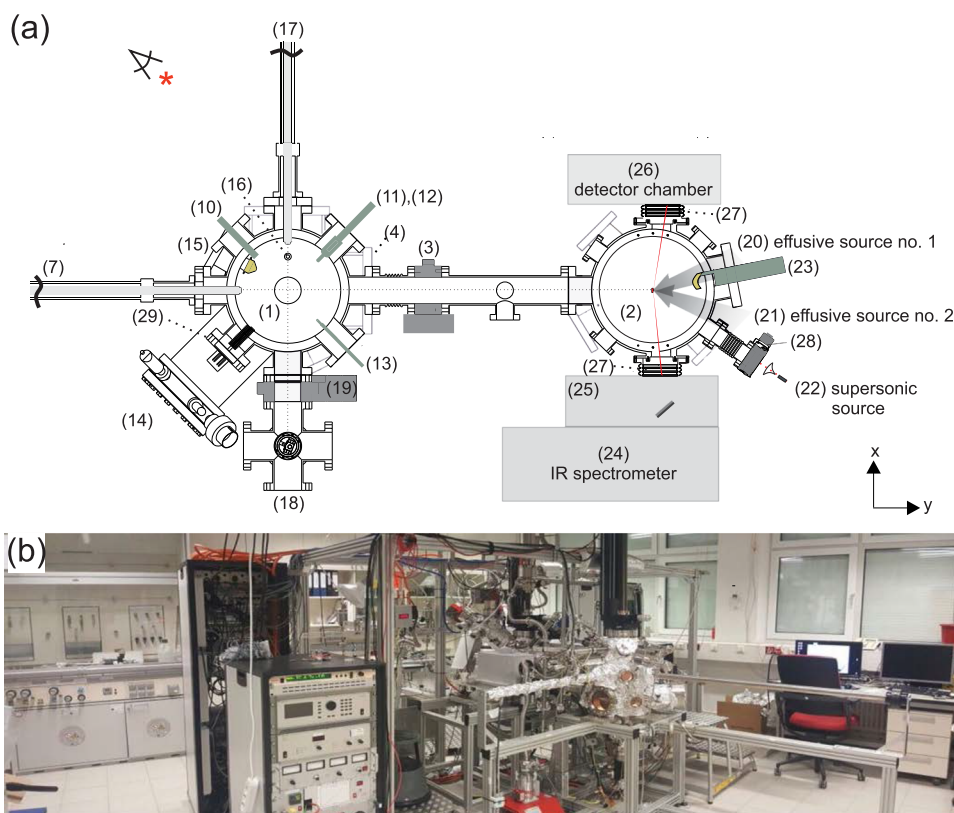


**FIG. 3.** (a) Schematic top view of the experimental setup showing the preparation chamber, the reaction chamber, and the APC. The cut-out was done slightly above the plane created by the transfer rods, and for a better visibility only the lower part is shown. The labeled components are (1) preparation chamber, (2) reaction chamber, (3) gate valve, (4) flange for the TMP assembly of the preparation chamber, (7) magnetic transfer rod, (10) gas doser, (11) and (12) metal evaporators, (13) QCM, (14) LEED/AES, (15) QMS in the preparation chamber, (16) shutter assembly (17) magnetic transfer rod, (18) APC, (19) gate valve, (20) effusive source no. 1, (21) effusive source no. 2 (22) supersonic source, (23) QMS in the reaction chamber, (24) IR spectrometer, (25) external UHV adaptation chamber of the IR spectrometer, (26) IRAS detector chamber, (27) flexible bellows for IRAS assembly, (28) gate valve, and (29) ion gauge. The effusive sources are shown schematically with perspective arrows (20) and (21) as they are inclined and positioned above this plane. (b) A photograph of the experimental setup. The perspective is marked in (a).

see also Fig. 3(a) (23), Hiden, Hal/3F 301 PIC system type 553201]. The QMS is additionally equipped with a gold-plated shutter [Fig. 5 (5)], which protects the QMS from detecting the gaseous species directly scattered from the sample surface to the ionization region of the mass spectrometer, as well as with a differential

pumping stage (pumped by a TMP Leybold, Turbovac SL-80). A gold-coated shutter [Fig. 5 (6)] driven by a UHV stepper motor [Fig. 5 (7), AML, D35.1] can be placed in front of the sample for performing sticking coefficient measurements. IRAS experiments are performed by means of a vacuum FT-IR spectrometer which has been modified to meet the special requirements of the beam experiment [Fig. 3(a) (24)–(26), Bruker, Vertex 80v]. This includes an external UHV adaptation chamber [Fig. 3 (25), Bruker, W109/UHV Vertex v80v] and a detector chamber [Fig. 3 (26)]. The spectrometer [Fig. 3 (24)] is equipped with an internal detector—Deuterated L-alanine Doped Triglycerine Sulfate (DLA-TGS), (Bruker, D301/B)—which is placed inside the spectrometer compartment and used as an internal reference for qualitative and quantitative sampling of the IR transmission in the spectrometer setup. The spectrometer is pumped by a scroll pump (EDWARDS, nXDS10i), and the typical base pressure in the spectrometer chamber is less than 1 mbar.

The circular apertures in the spectrometer were replaced by  $1.2 \times 6$  and  $0.7 \times 4$  mm<sup>2</sup> aperture slits to modify the beam profile at the sample position to the required rectangular geometry, which fits the rectangular shape of the sample. Once the IR beam exits the spectrometer, it enters the external chamber [Fig. 3 (25)] where it is focused onto the sample by a parabolic mirror with a focal length of 250 mm. The incidence angle amounts to be 83° with respect to the sample surface normal. Only the p-polarized component of the IR beam produced by the mid-infrared (MIR) p-polarizer (Bruker, F351) is used in the measurements to improve the signal-to-noise ratio. The reflected beam enters the detector chamber

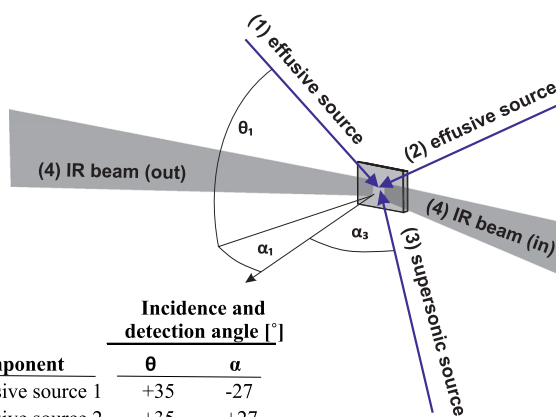


**FIG. 4.** Schematic representation of the orientation of the molecular and infrared beams with respect to the sample. Beam and detector geometries are given in the inset table. All angles are given with respect to the surface normal.

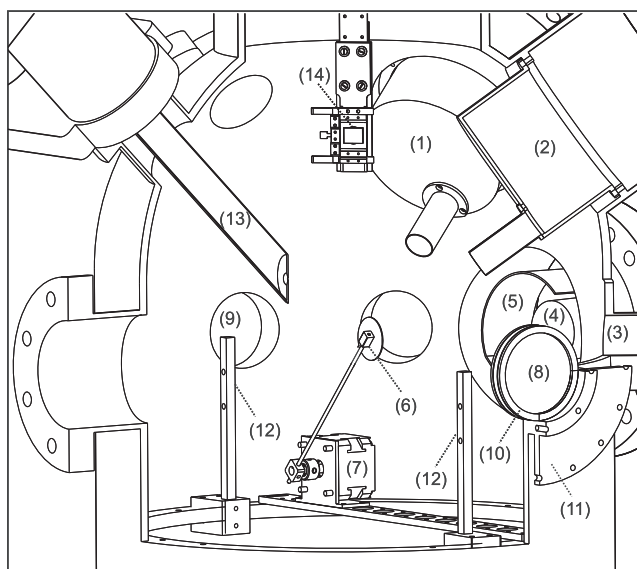


**FIG. 5.** Schematic drawing of the reaction chamber. The labeled components are (1) and (2) effusive source nos. 1 and 2, respectively, (3) flange for the supersonic beam source, (4) QMS, (5) Au coated shutter for QMS, (6) Au plate sample shutter, (7) stepper motor, (8) and (9) KBr windows for IRAS assembly, (10) Viton gasket, (11) flange for bellow assembly (12) center-position alignment pins, (13) beam monitor, and (14) movable sample plate and sample holder.

[Fig. 3 (26)], and it is focused by an ellipsoid mirror with a focal length of 250 mm onto the liquid-nitrogen cooled MCT detector. The detector chamber is pumped by a pumping station (Pfeiffer, HiCube 80 Eco with a backing diaphragm pump MVP-15-4) to reduce contribution of water ice, irreversibly accumulating on the cooled MCT detector, that might interfere with the measurements. The typical base pressure in the detector chamber is  $5 \times 10^{-5}$  mbar. The reaction chamber is separated from the IR spectrometer and detector chambers by KBr windows [Fig. 5 (8) and (9)] and sealed by Viton gaskets [Fig. 5 (10)]. The spectrometer vacuum flanges enclose the UHV flanges of the reaction chamber [Fig. 5 (11)] and act as a differential pumping stage. The reaction chamber is connected to the detector chambers and the external chamber of the spectrometer via two flexible bellows which are sealed by Viton O-rings [Fig. 3(a) (27) and (28)]. Both the spectrometer and the detector chamber are mounted on stable movable Al-platforms (Rose + Krieger) equipped with an xyz translator which enables a quick removal and precise reconnection of the spectrometer and the detector.

The determination of the sample-center position, i.e., the calibration of all four coordinates of the sample in space ( $x$ ,  $y$ ,  $z$ ,  $\theta$ ) is realized by adjustment pins [Fig. 5 (12)], for details see Sec. II C 3 a), and the measurement of the distribution and the absolute molecular flux of gaseous species is performed by means of a molecular beam monitor [Fig. 5 (13)], for details see Sec. II C 3 b).

### 1. Effusive beams

The reaction chamber contains two effusive molecular beams that are designed to provide well-defined, constant, and

homogeneous flux of gaseous molecules and to allow the fast and variable modulation of the beam flux on a time scale of a few hundred milliseconds. The most important requirement to the molecular beams implemented in this setup is their compact size, which allows us to combine all required components—two effusive and one supersonic molecular beams as well as the infrared setup—in one reaction chamber.

A cross section of the effusive molecular beams is shown in Fig. 6(a). The setup of the effusive molecular beam includes two chambers (DN 100 CF-F) providing two differential pumping stages separated by a 15 mm circular aperture (1). The first differential stage [(2)-inner pumping stage] is pumped by a 260 l/s TMP (Pfeiffer, HiPace 300) mounted at flange no. (3), and the second differential stage [(4)-outer pumping stage] is pumped by the same type of TMP and it is mounted at flange no. (5). The latter pumping stage is constructed as an integral part of the reaction chamber (6), to maximize the pumping speed and to minimize the distance to the exit beam orifice [not shown, see Fig. 5 (1) and (2)]. The pressure of both differential stages is measured by cold cathode pressure gauges [(7), Pfeiffer, IKR 361]. The effusive expansion is produced by employing a glass capillary array (GCA, Collimated Holes, Inc., holes size  $50 \mu\text{m}$ , holes density  $2 \times 10^6$  holes/cm<sup>2</sup>, 1 mm thickness) (8) which is mounted on the source tube sealed by Teflon gaskets (9) and is connected via a stainless-steel hose to the gas inlet flange (10). The source tube is fixed to the inner walls of the first pumping stage via clamps (11) in which the center of the GCA and the aperture are positioned in the same axis. The distance of the GCA to the sample position can be adjusted by varying the position of the GCA in the tube. The GCAs of sources 1 and 2 are located 378 and 368 mm away from the sample surface, respectively. The inner pumping stage is mounted on a flexible bellow (12) and can be adjusted by two orthogonally arranged translator-screws (13) operated by translation feedthroughs (14), which are used for beam alignment. After exiting the inner pumping stage through the aperture of 15 mm, the molecular beam enters the outer pumping stage, where it can be interrupted or opened by means of shutter (15). The beam shutter is a rectangular sheet of Al metal plate, which is driven by a UHV-compatible stepper motor [(16), AML, D35.1]. The shutter is fully remote controlled (using LABVIEW software) and allows arbitrary opening times of at least 150 ms.

Finally, the required backing pressure for the GCAs is typically 0.001–1 mbar. Two gas lines which are part of a dedicated manifold gas system are connected to the tubes that deliver gas to the GCAs and can be evacuated through TMP (Pfeiffer, HiPace 80) or scroll pump (EDWARDS, nXDS10i). Each of the lines has an electropneumatic angle valve (novotek, 706142) allowing for fast switching of the gas used to generate molecular beam as well as complex gas mixture. The pressure in the gas line is measured by a capacitance manometer (MKS Baratron 627D, readable pressure range  $5 \times 10^{-4}$  to 1 mbar) and is regulated and stabilized by a flow control valve (MKS 248 A) equipped with a PID pressure controller (MKS Type 250).

### 2. Supersonic source

Figure 7 shows a schematic of the supersonic source. The source is an independent UHV system which is separated from the reaction chamber via gate valve [(1), see also Fig. 3(a) (28)]. The source consists of an expansion chamber, which is pumped by 2100 l/s turbo

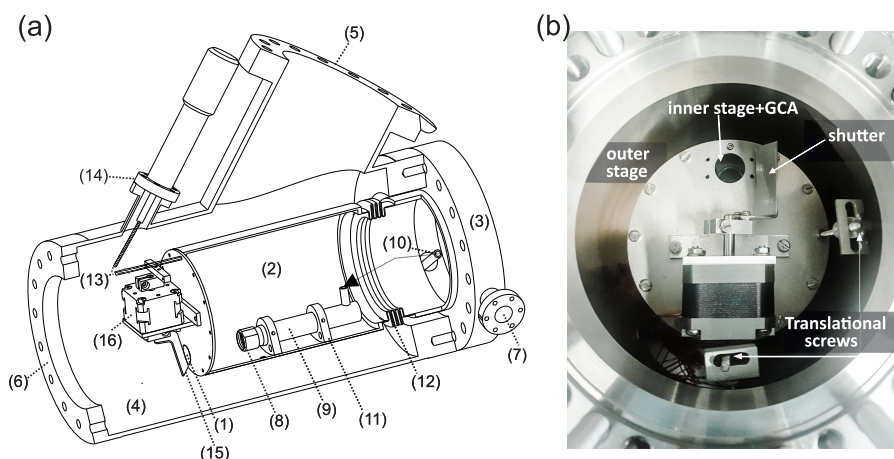


**FIG. 6.** (a) Effusive beam source. For a better visibility, a cut-out of the outer and the inner stage shows only the back half of the source. The actual setup contains an additional translational screw and feedthrough and a flange for the pressure measurement of the inner stage. The labeled components are (1) beam inner aperture, (2) inner pumping stage, (3) flange for TMP of the inner pumping stage, (4) outer pumping stage, (5) flange for TMP of the outer pumping stage, (6) flange connected to the reaction chamber, (7) pressure measurement, (8) GCA, (9) source tube, (10) gas inlet, (11) clamps for GCA assembly, (12) flexible bellow, (13) translational screw, (14) translational feedthrough, (15) shutter, and (16) stepper motor. (b) Top view photograph of the effusive source.

molecular pump [(2), Leybold, MAG integra], and two differential pumping stages pumped by 590 l/s and 65 l/s turbo molecular pumps [(3) and (4) Leybold, MAG w 700, TURBOVAC 80 H]. As a backing pump, a rotary vane pump is utilized (25 l/s, Leybold, SOGEVAC® SV28 BI). The supersonic expansion is generated from a solenoid type pulsed valve with an orifice diameter of 100  $\mu\text{m}$  [(5), Parker, General Valves Series 9]. The pulsed source is driven by a controller allowing a minimum pulse width of approximately 150  $\mu\text{s}$ . The pulse valve is mounted on a xyz- translator allowing both vertical and

horizontal alignment of the propagating jet with respect to the molecular beam axis defined by the skimmer [(6), travel length 50 mm, MDC, EPSM-1502]. From the expansion, a molecular beam is extracted by means of a 0.7 mm skimmer [(7), made of nickel, Beam Dynamics, Inc.]. In the second differential pumping stage, the beam can be modulated by a beam shutter (8) and a mechanical chopper (9). The beam shutter is driven by a UHV compatible high-torque stepper motor (Oriental Motor, PKP268MD28B). The chopper wheel is machined from a 150 mm diameter Al disk and

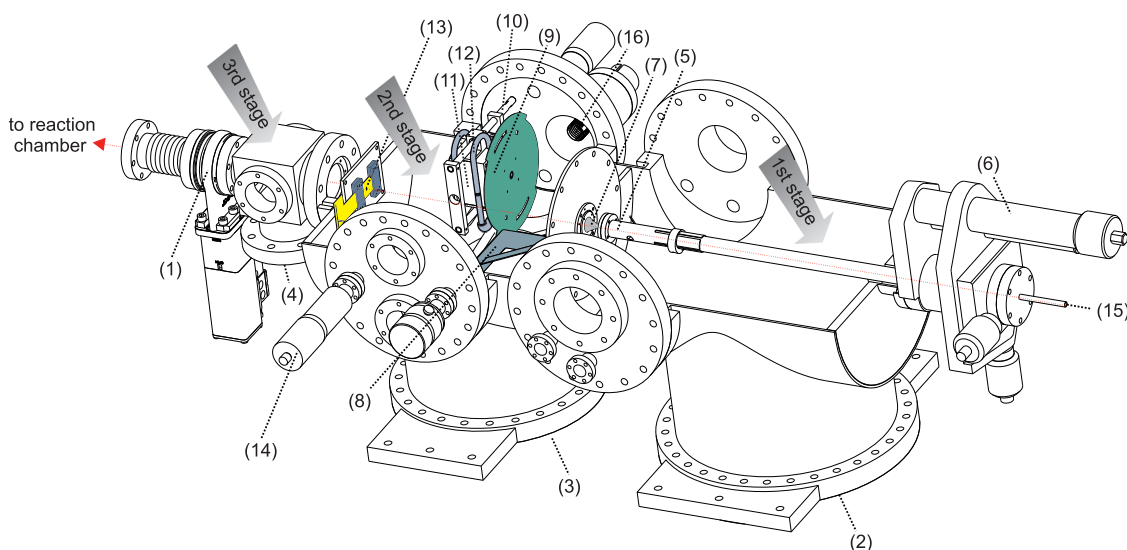


**FIG. 7.** Supersonic beam source. The labeled components are (1) gate valve, (2)–(4) flanges for TMPs, (5) pulse solenoid valve assembly, (6) XYZ-translational stage of the supersonic jet, (7) skimmer, (8) shutter, (9) chopper, (10) chopper translational stage, (11) chopper motor, (12) chopper cooling housing, (13) apertures, (14) aperture translational stage, (15) gas inlet, and (16) pressure gauge.

is mounted on the translation stage operated from the atmospheric side [(10), VAB, ML 16-50]. The chopper wheel is driven by a 400 Hz AC synchronous motor [(11), Globe motors, 75A1008-2], which is controlled by an AC frequency transformer. The motor assembly is clamped into a water-cooled Cu bronze block providing constant temperature operation conditions (12). The chopper can be modulated with different duty cycles allowing us to pass through 5%, 20%, or 50% of the original beam flux.

To reduce the pulse width and improve the pulse shape in pulsed valve operation, the rotating wheel chopper can be synchronized with the solenoid valve. This is done by dividing the synchronization signal by a 1/N counter to the desired pulsing frequency and externally triggering the valve controller after a delay time which is chosen such that a suitable slice of the pulse is cut out by the chopper wheel. In the current design, the chopper sample distance is 637 mm. Before hitting the sample surface, the beam passes through a square aperture, which determines the beam shape at the sample position. It is located in between the second and the third differential pumping stage to reduce the gas load in the third pumping stage. We can choose from three different square apertures of 2.5, 3.5, and 4.5 mm size on a Cu bronze blade (13). The aperture position is adjusted from the air side by moving the blade via a linear translator [(14), VAB, ML 16-50]. Due to the incidence angle of 35°, the beam profile at the sample is rectangular with an axial ratio of 1.2 and the beam size can be chosen to be smaller or larger than the sample, as well as the same size of the sample.

Finally, typical pressures of 1200–5000 mbar are delivered to the pulse solenoid valve through a 6 mm tube (15) to generate the supersonic expansion. The tube is connected to the manifold gas system, and the pressure measurement is realized by a capacitance manometer (10000 mbar, MKS, 722B14MFE2FA).

### 3. Adjustment tools and calibration procedures

To enable simultaneous kinetic and spectroscopic measurements, all molecular beams and infrared beam should be crossed at the same point on the sample surface. To fulfill this requirement, two adjustment and calibration tools were implemented: (i) adjustment pins for the determination of the sample center position and the position of the molecular beam monitor and (ii) molecular beam monitor for adjusting the positions of the molecular beams and determination of their spatial distribution and the molecular flux.

*a. Tools for adjusting the sample position.* To adjust the sample position in the reaction chamber, four cuboid metal-pins were installed on a narrow ring welded to the chamber along the internal perimeter. In front of each pin, a view-port is installed. The combination of these pins allows us to build two optical axes oriented at 45° with respect to each other, which intersect at the center of the chamber and allow for the calibration of all four coordinates of the sample in space, including the x, y, and z positions as well as the angle with respect to the position of the infrared beam. One pair of the pins building an optical axis parallel to the orientation of the surface plane of the sample is shown in Fig. 5, the pins are indicated as (12).

The positions of the IR spectrometer and the detector with respect to the chamber and to each other are determined by a support frame, at which both parts of the spectrometer are installed. The spectrometer and the detector chambers are connected to the

chamber via flexible bellows sealed by Viton O-rings. The fine tuning of the position of the infrared beam is performed by adjusting the mirrors of the spectrometer to maximize the signal reflected from the sample, which is installed at the center position of the reaction chamber. The rough alignment can be done using visible light, while the final adjustment of the mirror positions is performed by employing an infrared source.

*b. Tools for adjustment of molecular beams and molecular flux measurements: Molecular beam monitor.* Molecular beam monitor is employed for two purposes: (1) adjustment of the molecular beams to the correct position in space, enabling crossing of all three molecular beams at the center of the sample, and (2) determination of the absolute molecular flux and the beam profile, containing information about the spatial distribution of gaseous species entering the reaction chamber.

The molecular beam monitor implemented in this apparatus [Fig. 5 (13)] is based on the principle of an accumulation detector that is an adaption of the beam monitor described previously.<sup>27</sup> The beam monitor contains a high accuracy ion gauge (Granville-Phillips, 370 Stabil-Ion) mounted to a stainless steel tube 490 mm long with a diameter of 14 mm. At the front end of the tube, a stainless-steel plate is mounted, which has a 1 mm diameter hole in its center. This orifice allows the expanding gaseous molecules to enter the inner space of the tube. The pressure gauge measures the pressure rise upon this process, which can be linked to the absolute flux of the molecular beam, as described below. The assembly is mounted on a manipulator with three translational degrees of freedom (travel length 50 mm, MDC, EPSM-1502) allowing us to bring the molecular beam monitor—more specifically, the orifice—into exactly the same position, where the sample should be situated. In the working position, the beam monitor is positioned at the sample center position, which is calibrated in the same way as it is done for the sample position (see Sec. II C 3 a), and the incoming molecular beam enters the orifice of the beam monitor in 45° with respect to the orifice plane. By moving the molecular beam monitor in space, it is possible to measure the distribution of the beam intensity at different points in the chamber, which will be denoted as a beam profile in the following. By measuring the beam profile, the current position of the molecular beam in space can be determined. In order to adjust the beam position to the center point of the chamber, which is the position of the sample, and to reach a homogeneous distribution of the gaseous species over the sample, the inner pumping state of the effusive beams [Fig. 6(a) (2)] including the glass capillary array [Fig. 6(a) (8)] can be moved with respect to the outermost beam aperture [Fig. 5 (1) and (2)], by using two orthogonally arranged translational screws operated with translational feedthroughs [Fig. 6(a) (13) and (14) and “translational screws” in Fig. 6(b)].

For the supersonic molecular beam, the adjustment procedure involves initially the adjustment of the position of the pulsed source from the skimmer along the beam path. The skimmer is mounted at a fixed position at the exit of the first pumping stage [Fig. 7 (7)]. The exact pulsed source-skimmer distance is less crucial, but it must be far enough to ensure the transition to molecular flow in front of the skimmer as well as reducing effects such as backscattering from the skimmer.<sup>28</sup> The pulsed source assembly is mounted on a manipulator with three translational degrees of freedom allowing us to set the

required translation precision along the beam line. The horizontal and vertical alignment of the pulse valve is optimized by maximizing the detected beam intensity using the beam monitor positioned along the beam line. To adjust this beam position to the center point of the chamber, the beam monitor is placed at the center in the same way as it is done for the sample position. The supersonic beam setup is positioned on movable support frame, and it is connected to the reaction chamber via flexible bellow. Its position with respect to the center position can be adjusted by using four translational screws. Finally, a fine adjustment is performed to set the position of the beam apertures located at the exit of the second pumping stage with respect to the center position [Fig. 7 (13)]. For this, the frame carrying the aperture plate can be linearly moved inside the molecular beam by using a linear translational feedthrough connected to the frame [Fig. 7 (14)].

A successful adjustment of all three molecular beams should result in a homogeneous and symmetric distribution of the gaseous species at the sample position.

The molecular beam entering the aperture causes a pressure rise inside the detector volume. After equilibration of the incoming/outgoing effusive flux to/from the detector volume, a constant pressure is reached that can be used to calculate the absolute beam flux by the following relation:<sup>29</sup>

$$\text{Flux} = \frac{dN_{\text{out}}}{A \cdot dt} = \frac{p}{\sqrt{2\pi M k_B T}},$$

where  $N_{\text{out}}$  is the number of molecules passing the beam monitor aperture with cross-sectional area  $A$ ,  $p$  is the pressure rise in the detector volume,  $M$  is the mass of the molecule,  $k_B$  is the Boltzmann constant, and  $T$  is the temperature of the detector. The high stability pressure gauge has an accuracy of 4% and a repeatability of 3%. Typically, the background pressure in the detector is about  $2 \times 10^{-8}$  mbar, so the minimum detectable pressure rise is  $\sim 8 \times 10^{-10}$  mbar. For Ar, this corresponds to a resolution of the molecular beam flux amounting to about  $2 \times 10^{11}$  molecules  $\text{cm}^{-2} \text{s}^{-1}$ .

#### D. Sample transfer system and sample holder design

The movable sample plate designed for this apparatus allows for a rapid transfer of the sample between different chambers. The sample can be heated and cooled in a broad temperature range (95–1300 K), which is required for the preparation of various model catalytic surfaces—both metal single crystals and epitaxially grown thin oxide films. Each of the three manipulators implemented in three UHV chambers is equipped with a sample holder allowing for effective cooling, heating, and precise temperature control. The temperature measurement is realized by using a K-type thermocouple; the sample can be additionally connected to the high voltage supply, which is required for the deceleration of the metal ions during metal evaporation onto the sample surface. While the sample holders are identical in the preparation and the reaction chambers, in which electron beam heating is used for temperature control, the design of the sample holder in the APC was changed as the electron bombardment cannot be applied under ambient pressure conditions. For this reason, a ceramic button heater was implemented in the APC (the details will be described in Sec. II E).

Figure 8(a) shows side-, back-, and front-view of the *movable sample plate*—the movable compartment which is directly attached to the sample—and Fig. 8(b) shows a front view of the sample holder—the fixed assembly attached to the manipulators of the different chambers. The fixed assembly surrounded by the dashed lines in Fig. 8(b) will be denoted as the *sample holder adaptor* (10) in the following.

In the *movable sample plate* [Fig. 8(a)], single crystal sample (1) is mounted on Mo supporting plate (2). The metal single crystal samples are cut in the form of a square  $10 \times 10$  mm with a thickness of 1–2 mm, which are spot welded to the Mo supporting plate via tantalum foils (3). The Mo supporting plate has a central opening with a diameter of 8.5 mm allowing access to the back side of the sample. A rectangular ceramic plate containing six in-line holes (4) is attached via its center—or more specifically its two central holes—to the front side of the supporting plate by means molybdenum screws (5) and a trapezoid pin (6). The other two pair of holes are used for the installation of Chromel-Alumel thin thermocouple sheets from both front sides of the supporting plate (7) and (8) via additional screws and trapezoid pins. The ceramic plate ensures an electric insulation between the thermocouple pair and the Mo supporting plate. The trapezoid form of the pins was chosen to realize a sandwichlike arrangement, in which the probability of an unwanted electrical contact caused by thermal expansion of individual trapezoid pins during heating is minimized [side view, Fig. 8(a) (6)].

Thermocouple wires are pressed with the molybdenum screws against the thermocouple sheets [(7) and (8)] and are spot welded to the edge of the single crystal from the front side of the supporting plate (not shown). This assembly allows for the accurate temperature measurement on the single crystal (1) and not on the supporting plate (2) of the *movable sample plate*.

The *sample holder* [Fig. 8(b)] includes four identical tangential trapezoid pins (9) with each of them containing two threads. This arrangement of the pins and screws is employed to fix the *movable sample plate* to the *sample holder adaptor* (10) for manipulators I and II [see Fig. 2 (5) and (6) or Fig. 9 (4) for the manipulator of the APC]. For this purpose, the *movable sample plate* slides into the space between the thin tantalum foil (11) attached by the tangential trapezoid pins (9) to the *sample holder adaptor* (10), while the thermocouple sheets [(7) and (8) attached to the Mo supporting plate (2), Fig. 8(a)] slide into the thermocouple sheets [(12) and (13) installed on the sample holder adaptor (10)]. The latter contact allows for the temperature control of the sample. To ensure temperature measurements on the sample only, two ceramic plates are inserted in between the sample holder adaptor (10) and the thermocouple sheets (12) and (13). Finally, the *movable sample plate* can be attached to the *sample holder* using magnetic transfer rods [VAB, MDS 40-1200, VAB, MDS 40-700, see Fig. 3(a) (7) and (17)] containing an adaptor with rotating locking mechanism which is attached to the clamp of the *movable sample plate* (14). A photograph of the *movable sample plate* inserted into the *sample holder* of the manipulator in the reaction and preparation chambers is shown in Fig. 8(c) with the same labeling of the components shown in Figs. 8(a) and 8(b).

Figure 8(d) shows a schematic drawing of the *sample holder* mounted onto the manipulator of either the reaction or the preparation chamber. Since the manipulator has an electrical contact to the UHV chamber, the *movable sample plate* must be electrically insulated from the chamber potential. This is realized by

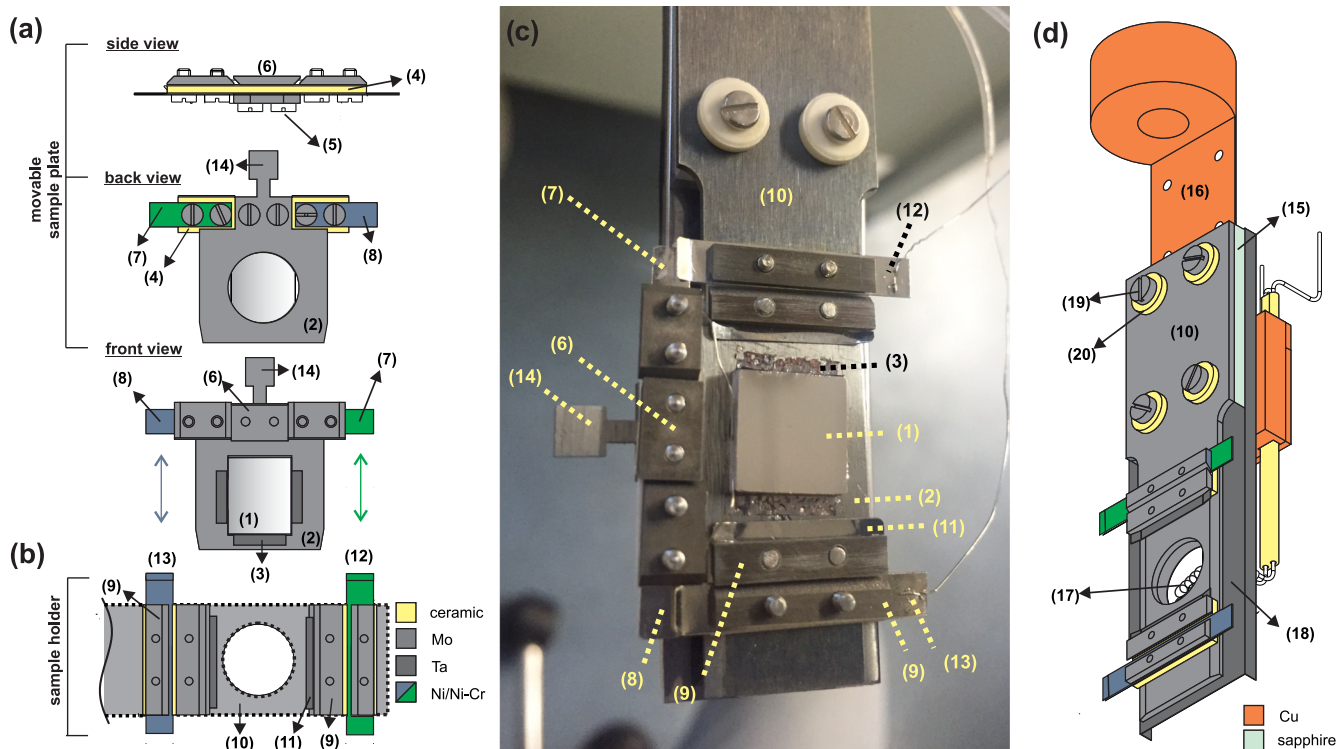


**FIG. 8.** (a) Schematic drawing of the *movable sample plate* from different perspectives and (b) the *sample holder* (top view), which is used to fix the *movable sample plate* on the manipulators of the reaction and preparation chambers. The legend indicates the color-coded materials of the sample plate and holder. (c) A photograph of the *movable sample plate* and the *sample holder* mounted on the manipulators in the preparation and reaction chambers. (a)–(c) *Movable supporting plate*: (1) single crystal (sample), (2) Mo sample supporting plate, (3) foil for sample assembly to the supporting plate, (4) rectangular plate containing six in-line holes, (5) screws, (6) trapezoid pins, (7) and (8) thermocouple thin sheets installed on the ceramic plate; *sample holder*: (9) tangential trapezoid pins, (10) *sample holder adaptor*, (11) thin foil for *movable sample plate* assembly, and (12) and (13) thermocouple thin sheets installed on the *sample holder adaptor*. (d) Schematic drawing of the *sample holder* installed in the preparation and reaction chambers. Color-coded materials are the same as shown in (b), and additional colors are indicated in the legend. The labeled components are (15) insulating plate, (16) platform attached to the manipulator, (17) sample heating filament, (18) shield to minimize unwanted heating of the sample holder, (19) screws for adaptor assembly, and (20) hat-shape washers.

employing a sapphire plate (15), which is an electrical insulator, but a fairly good thermal conductor. The sapphire plate is introduced between the copper platform (16) mounted on the bottom part of the manipulator and the *sample holder adaptor* [(10), see also Figs. 8(b) and 8(c)].

Heating of the sample in the reaction and preparation chambers is realized via electron bombardment or thermal radiation from a handmade filament [(17) Thoriated tungsten, Goodfellow], which is situated approximately 10 mm behind the *sample holder* and is aligned parallel to the sample to ensure homogeneous heating. To ensure heating of the sample only and minimize unwanted heating of the *sample holder*, a Ta shield (18) is mounted on top of the copper platform of the manipulator and it is attached to the *sample holder adaptor* via the sapphire plate. It contains the same central opening of the sample holder and the sample plate, and it is positioned in such a way that the openings are aligned. Finally, electron bombardment is realized by applying high voltage onto the sample via Ta wire which is pressed against the adaptor (10), see also Figs. 8(b) and 8(c) using Mo screws (19). The latter are electrically insulated from the chamber by hat-shape ceramic washers (20). In this setup, sample

temperature above 1400 K can be obtained upon heating via electron bombardment. In addition, when LN<sub>2</sub> flows through the coils in the manipulation stage, heat is efficiently removed from the sample and a temperature as low as 95 K is reached. The radiative heater in this setup can heat the sample up to 500 K.

### E. Ambient pressure cell (APC)

The APC (Fig. 9) is built based on a 6-way cross (DN 63 CF-F), which is separated from the preparation chamber by a gate valve [see also (3) in Figs. 2 and 3(a)]. It is pumped via a pumping station (Pfeiffer, HiCube Eco 300H) equipped with a turbomolecular pump (HiPace 300H, 260 l/s) and 3-stage diaphragm pump (MVP 030-3DC). The base pressure is measured with dual gauge (Pfeiffer, PKR 361). Figure 9(a) shows an overview of the APC and the flange housing; the enlarged cross section view is shown in Fig. 9(b). The APC consists of a platform [Fig. 9(a) (1)] mounted onto the upper flange of the 6-way cross (2) via 3 mm stainless steel tubes (3). The platform fulfills two rolls: (i) it serves as a reservoir for liquid nitrogen that can be filled through the tubes (3) from the air side and (ii) it serves as a

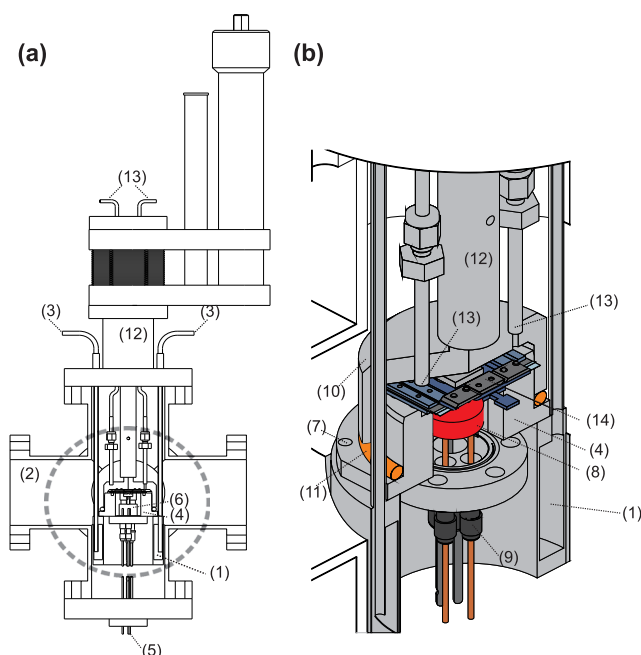


**FIG. 9.** (a) Cross section showing the ambient pressure cell setup. The experiments consist of a two-level system that combines UHV chamber with an elevated pressure reactor (encircled). (b) Enlarged view of the encircled part of (a). The labeled components are (1) platform for *sample holder* assembly (2) 6-way cross, (3) inlet/outlet platform cooling (4) *sample holder adaptor*, (5) electrical feedthroughs, (6) sample heating assembly, (7) screws of sample holder assembly (8) button heater (9) electrical feedthroughs, (10) metal cup, (11) Viton seal, (12) metal cup manipulator, (13) gas inlet/outlet, and (14) movable sample plate.

support for the *sample holder adaptor* (4). The bottom flange of the 6-way cross contains all electric feedthroughs (5) which are in electrical connection with the sample heating assembly (6). The *sample holder adaptor* has a hatlike shape, and it is positioned on top of the platform and fixed with screws [Fig. 9(b) (7)]. It has a central opening with a diameter of 8.5 mm allowing access to the back side of the sample. Heating is realized via a ceramic button heater [(8), Heat Wave Labs, 102273  $\varnothing$ .320" O2 Heater], which can be operated both under UHV and ambient pressure conditions. The sample is positioned directly on top of the heating ceramic button. Sample temperatures up to 1200 K can be reached with this resistive heater. The heating plate is manufactured of a catalytically inert ceramic material, which can be operated under the ambient pressure conditions. Before catalytic studies, reference experiments with inactive samples must be performed to quantify the possible contributions from the chamber walls to the overall reaction rate. The back part of the sample holder contains a custom flange accommodating the thermocouple and power feedthrough [(9), Ideal vacuum products, 108065, DN 16 CF-F]. Finally, the sample can be transferred from the preparation chamber directly into the sample holder of the APC by a magnetic transfer rod. When the *movable sample plate* is inserted into the *sample holder* of the APC, the cell can be sealed. This is realized by approaching a metal cup (10) toward the *sample holder* and pressing against a Viton sealing (11). The latter allows pressurizing

the APC while maintaining a high vacuum in the surrounding chamber, i.e., the 6-way cross [Fig. 9(a) (2)]. The metal cup is connected to a manipulator which is mounted on the upper DN 63 CF-F flange of the 6-way cross [(12), VAb, LDK 40-50]. The metal cup is also connected to two 3 mm tubes that are used as gas outlet and inlet (13). While using in the batch mode, they are connected to a metal bellow recirculation pump (Gasmot Ansysco, MB-41E). The recirculation loop is interfaced with GC (Agilent 7890B) through a pneumatic sampling valve. The GC is equipped with electronic pneumatic regulation inlet (Split/Splitless 0–100 PSI EPR Inlet, G4352-60502) and thermal conductivity and flame ionization detectors. To detect different types of hydrocarbons, the GC is additionally equipped with a fused silica capillary column (MACHERY-NEGAL, LIPODEX A, model 723360.50, internal diameter 0.25 mm, length 50 m). The batch mode, which is typical choice for studies on low surface area model catalysts, allows an easier detection of the products due to the increased reactants conversion with reaction time.<sup>30,31</sup> The gas pressure is measured using two absolute pressure transducers (full range 10 mbar and 1000 mbar, MKS, Baratron 627D).

### III. IMPLEMENTATION AND TEST MEASUREMENTS

#### A. Performance of the molecular beams

##### 1. Effusive beams

Prior testing the performance of the molecular beams, we performed their alignment to the sample center position as described in Sec. II C 3 a. Measuring the molecular flux and its spatial distribution requires a reliable measurement of the beam intensity and its profile. Figure 10(a) shows a top view photograph of the reaction chamber during beam intensity and distribution measurements.

Figures 10(b) and 10(c) show contour beam profiles of effusive source nos. 1 and 2, respectively, at a backing pressure of  $7.0 \times 10^{-2}$  mbar. For this measurement, the beam monitor was placed in the center position and moved in the plane parallel to the sample position ( $xz$  plane, see Fig. 2). The color map illustrates the pressure gradient measured with the beam monitor across the plane parallel to the sample position, and the dashed black rectangular indicates the area  $10 \times 10$  mm<sup>2</sup>, at which the sample will be situated in the center of the reaction chamber.

To obtain a homogeneous exposure during reactivity and IR absorption measurements, the outer beam diameter was chosen to be slightly larger than the sample (12 mm). Both beam profiles show an ellipsoid profile shape due to the inclination of the beams with respect to the sample surface plane (see the inset of Fig. 4). Taking into consideration the symmetric arrangement of the beams in space with respect to the center position, the beam profiles should appear symmetric in this representation, which was indeed observed experimentally.

When the beam monitor is moved during the measurement to scan the beam profile along the central plateau, the variation of the beam intensity corresponds to the stated repeatability of the gauge of 3% suggesting that a stable homogeneous flux of gaseous species is formed in an effusive expansion. The experimentally measured the variation of the beam intensity along the central axes of the sample amounts to approximately 4%.

A variable molecular beam flux can be achieved by varying the backing pressure of the beam source. Figure 11 shows the centerline

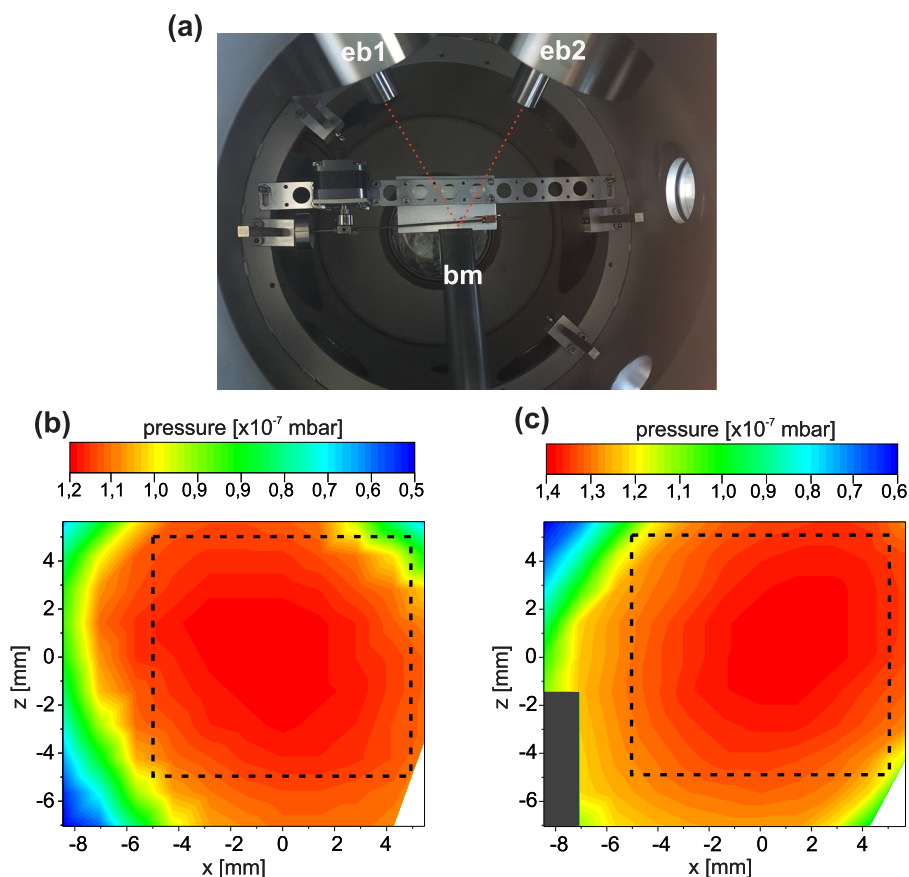


**FIG. 10.** (a) A photograph of the setup for beam profiling and flux measurements. All beam sources are aligned with respect to the sample position. (b) and (c) Molecular beam profiles at the center position of source nos. 1 and 2 obtained at the backing pressure of Ar amounting to  $7 \times 10^{-2}$  mbar. The dashed rectangles show the sample position with respect to the molecular beam. The sample position is parallel to the  $xz$  plane.

intensities of the two effusive sources recorded for Ar as a function of the backing pressure. For this measurement, the molecular beam monitor is placed exactly in the sample position. The intensities of the effusive sources were measured as a function of the backing pressure of the beam sources by varying the pressure over several orders of magnitude. The source pressures of source nos. 1 and 2 were measured with capacitance manometers with full scale range of 1 mbar (red squares and black circles). To test the pressure limit of the effusive source employed in our beam setup, the source pressure of source no. 1 was additionally measured with a capacitance manometer of 10 mbar range (MKS, Baratron 627D, green triangles).

It should be noted that the effusive beam expansion starts from low pressure conditions with nearly no interaction between gas phase particles so that this type of expansion is nearly gas independent. In the backing pressure range from  $1 \times 10^{-2}$  to 1 mbar, the molecular flux increases linearly with the increasing pressure. In this range, both beams show practically identical source pressure intensity behavior. The distances between the position of the beam orifice installed in the center position and the GCAs amount to 378 and 368 mm for the source no. 1 [Fig. 10(b)] and the source no. 2 [Fig. 10(c)], respectively, which accounts for the slightly different molecular flux at the same backing pressure of the effusive source. Above 1 mbar, scattering losses result in a decreasing intensity,<sup>29</sup>

and the flux levels off at a value of  $\sim 9.6 \times 10^{14}$  molecules  $\text{cm}^{-2} \text{s}^{-1}$ . This intensity corresponds to deposition of about 1.3 ML of CO molecules on Pt(111) per second. In principle, there is no lower limit to the beam intensity. However, the components of the source pressure regulation—the capacitance manometer—limit the range of controllable values of the molecular flux. In practice, a modulation of 0.1% monolayer can be obtained. It should be pointed out that in our current setup, the background pressure in the molecular beam detector limits the minimum detectable pressure change to  $\sim 2 \times 10^{11}$  molecules  $\text{cm}^{-2} \text{s}^{-1}$ . Variable time modulation of the molecular flux by means of a mechanical shutter allows the production of beam pulses of arbitrary length with the minimum pulse length of 150 ms. When the molecular beam is blocked by the shutter, a leakage of about 3% of the unblocked beam intensity is observed using the QMS, which is caused by the increased background pressure in the outer pumping stage.

## 2. Supersonic beam

The supersonic source is operated by a pulsed solenoid valve (see Sec. II C 2), which opens as a response on a current pulse through a solenoid, creating a magnetic field that lifts a plunger from the valve orifice. A typical voltage of 220 V and a current of 0.4 A were used to activate the valve, and typical opening times of

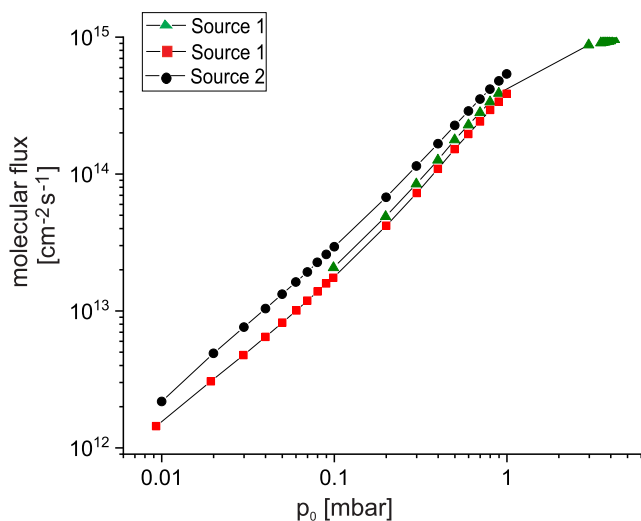


**FIG. 11.** Intensity of the effusive beam sources plotted as a function of the Ar backing pressure at 298 K. The pressure limit of source no. 1 was tested with additional pressure transducer.

200–300  $\mu\text{s}$  were obtained. The nozzle-skimmer distance of 185 mm was installed. The repetition rate of the pulse valve results in a maximum working pressure in the first stage of  $2 \times 10^{-6}$  mbar and  $2 \times 10^{-8}$  in the second stage. The aligning procedure for the supersonic beam includes (i) aligning the propagating jet with respect to the molecular beam axis defined by the skimmer, which is realized by installing the solenoid valve on an XYZ-translational stage providing a possibility to change the valve's position in three dimensions [(6) in Fig. 7], and (ii) aligning the jet that passed the skimmer with respect to the sample's center position in the reaction chamber. The latter alignment procedure is realized by adjusting the positions of the translational screws mounted on the platform supporting the supersonic beam. The molecular beam profile and the beam intensity were measured by the molecular beam monitor, which was placed at the center position of the reaction chamber, where it can be moved along the axes of the surface plane. The obtained 3D beam profile along the sample surface employing 4.5 mm inner aperture is shown in Fig. 12(a). The measured horizontal beam profiles for the three different apertures are shown in Fig. 12(b). The beam intensity at the center position amounts to  $\sim 2 \times 10^{13}$  molecules  $\text{cm}^{-2} \text{s}^{-1}$  for a back pressure of 1.710 bar Ar at 298 K and an average pulse time of 305  $\mu\text{s}$ . When the beam monitor is moved during the measurement to scan the beam profile along the central plateau, the variation of the beam intensity corresponds to the stated measurement repeatability of the gauge of 3%. This observation suggests a stable homogeneous flux of gaseous species formed in a supersonic expansion.

Depending on the experimental requirements, the beam can be chosen to be either the same size, larger, or smaller than the sample size by choosing one of three inner apertures [see Fig. 7 (13)]. The tails appearing at the sharp beam edges shown in Fig. 12(b) for different apertures are a result of a convolution of the beam monitor aperture (1 mm) with the actual beam profile.

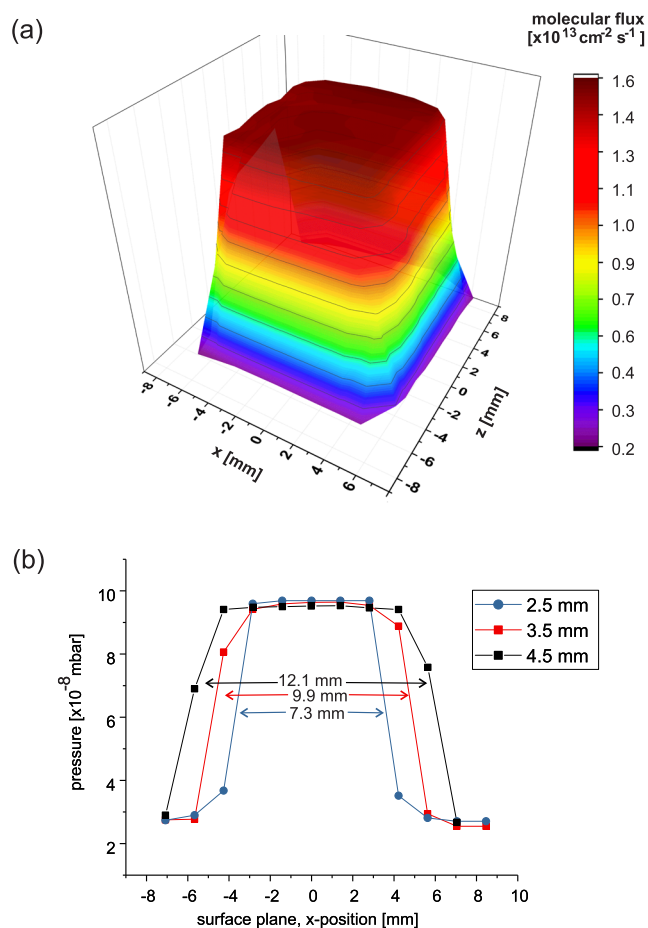


**FIG. 12.** (a) Beam profile at the center position obtained at a backing pressure of 1.710 bar and employing the 4.5 mm inner aperture. (b) Horizontal beam profile for different aperture sizes.

## B. Test measurements: Adsorption of acetophenone and (R)-(+)-1-(1-naphthylethylamine) on Pt(111)

In order to test the performance of the multimolecular beam/spectroscopy apparatus, interaction of two adsorbates—*acetophenone* and (R)-(+)-1-(1-naphthylethylamine) (R-NEA)—with Pt(111) was studied as a detailed function of coverage. Both compounds were previously investigated in adsorption studies on either powdered materials or single crystals, allowing us to directly compare the test results with the previously published data.

The Pt(111) sample was cleaned prior to acetophenone exposure in the preparation chamber by a series of cycles consisting of Ar sputtering (20 min, beam energy 1 kV at  $5 \times 10^{-6}$  mbar Ar), subsequent annealing at 850 K in  $\text{O}_2$  ( $5 \times 10^{-6}$  mbar, 20 min) followed by annealing under UHV conditions (1300 K, 2 min). The last cleaning step included reduction with CO ( $5 \times 10^{-6}$  mbar) at 400–450 K and subsequent flashing to 600 K. The surface structure and cleanliness of the sample surfaces were examined by LEED and AES. Additionally, IR spectra of adsorbed CO were obtained

to check the availability and distribution of the different adsorption sites on Pt(111).

### 1. Adsorption of acetophenone: Characterization of high vapor pressure adsorbates

Acetophenone was deposited via an effusive molecular beam onto Pt(111) at 115 K while IR spectra were recorded during the exposure. Figure 13 shows a series of IR spectra obtained at 115 K in the coverage range between 0.1 and 10 ML. With increasing exposures, continuously growing intensities of all vibrational features are observed confirming the formation of acetophenone ice. The IR spectra recorded for the multilayer coverages serve as a reference for molecular adsorbates, which are largely unperturbed by the interaction with the underlying metal support. The lowest spectrum is related to the IR gas phase spectrum of acetophenone<sup>32</sup> and is shown for comparison.

Based on the previous assignment of the vibrational band performed for the acetophenone gas phase spectrum,<sup>33</sup> most of the vibrational bands in the acetophenone multilayer can be identified. The most intense band at  $1683\text{ cm}^{-1}$  is related to the C=O stretching vibration. The bands at  $1598$  and  $1583\text{ cm}^{-1}$  are assigned to the in-plane C-C stretching modes of the aromatic ring. The bands at  $1431$  and  $1362\text{ cm}^{-1}$  are related to the antisymmetric and symmetric methyl deformation, respectively. The strong absorption band at  $1263\text{ cm}^{-1}$  is assigned to the x-sensitive benzene mode.<sup>33</sup> The band at  $958\text{ cm}^{-1}$  is related to the mix modes comprising the  $-\text{CH}_3$  rocking and the aliphatic C-C stretching.

Having identified the vibrational bands related to the unperturbed molecules in the multilayer, we can now assign the bands observed for the submonolayer coverages, which might be potentially strongly perturbed by the interaction with Pt. For this purpose, detailed coverage dependence of the IR spectra was obtained allowing us to follow the evolution and possible frequency shifts of all bands when reducing the coverage from multi- to submonolayer range (shown in the upper part of Fig. 13).

It can be clearly seen that the spectra obtained for the submonolayer coverages exhibit generally the same vibrational bands as

the spectrum obtained for the multilayer yet show a different intensity distribution. This difference in the intensities results most likely from a specific adsorption geometry of acetophenone at the metal surface, which affects the relative ratio of the intensities due to the metal surface selection rule.<sup>25</sup>

### 2. Adsorption of R-NEA: Characterization of low vapor pressure adsorbates

R-NEA was used to test the experimental setup for the deposition and spectroscopic characterization of low vapor pressure adsorbates that cannot be deposited via the molecular beams.

After cleaning, the Pt crystal was transferred to the deposition chamber [bottom part of the preparation chamber, see Fig. 2 (8)]. R-NEA was dosed on Pt(111) at 155 K via backfilling, and then the sample was transferred to the main chamber for the acquisition of the IR spectra.

The requirement of integrating a dedicated deposition chamber for the deposition of low vapor pressure organic compounds, in order to keep the reaction chamber as clean as possible, results in fundamental question concerning the stability of the measurement and background collection. The background spectrum is a single channel spectrum acquired at the pristine metal surface to account for the contributions of the instrument and the environment. In the standard procedure normally applied for the high vapor pressure compounds, the background is collected prior data acquisition with the sample being situated at the sample center position and then the adsorbates of interest are dosed at the sample via the molecular beams. This procedure does not require moving the sample and results in spectra exhibiting stable background. In contrast, the deposition of the low vapor pressure compounds cannot be realized via the molecular beams and therefore the sample must be moved to the deposition chamber. However, moving the sample away after collecting the background spectra results in unstable and wavy baseline, which falsifies the peak information.

In order to overcome these limitations, we developed a new procedure allowing to us obtain high quality IR spectra even for low vapor pressure compounds. For this, the sample is first cleaned

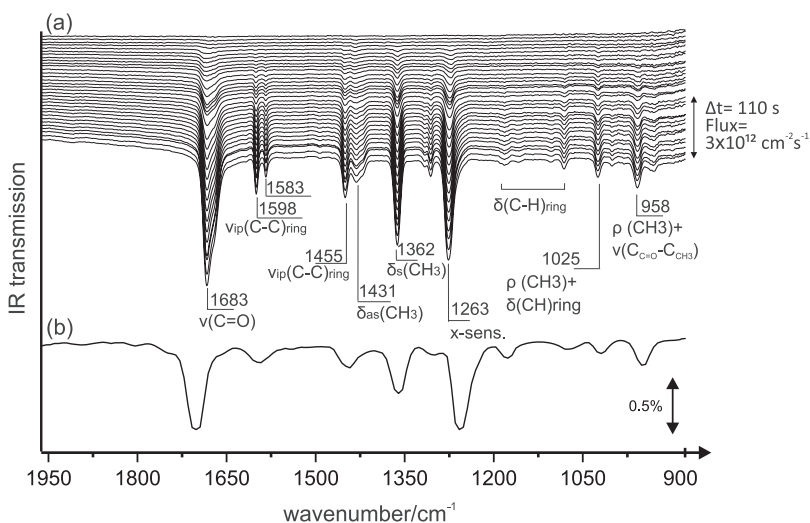
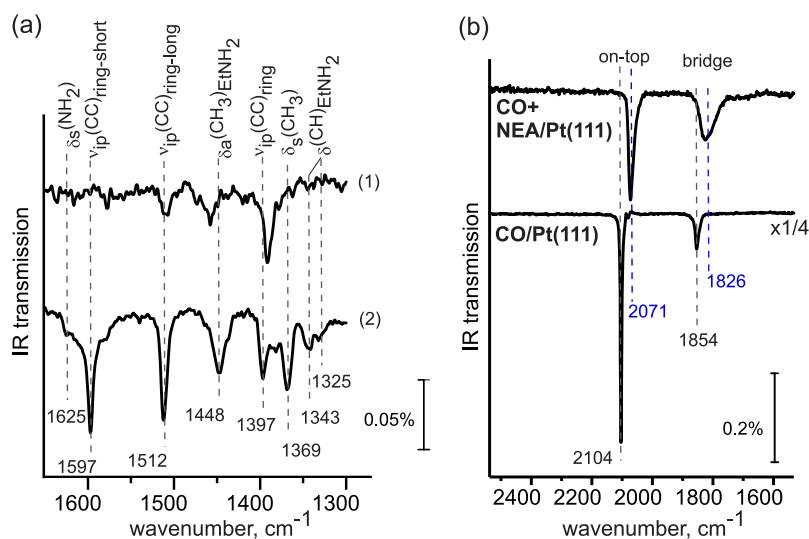


FIG. 13. (a) IR spectra recorded during the deposition of acetophenone flux onto Pt(111) at 115 K via beam source 2. (b) IR spectrum of acetophenone in the gas phase from NIST.<sup>32</sup>



**FIG. 14.** (a) IRAS spectra of R-NEA adsorbed on Pt(111) at 155 K: exposure  $5 \times 10^{-8}$  mbar for (1) 2 and (2) 10 min. (b) IRAS spectra of CO adsorbed on pristine Pt(111) and R-NEA/Pt(111) recorded at 155 K, CO exposure:  $6 \times 10^{14}$  molecules  $\text{cm}^{-2}$ . The R-NEA-covered surface corresponds to R-NEA exposure of  $5 \times 10^{-8}$  mbar for 2 min at 155 K.

in the preparation chamber and then the adsorbates of interest are deposited onto the sample in the deposition chamber. The sample is then transferred to the reaction chamber, and the IR spectrum is acquired. This spectrum is a single channel spectrum, which is still not divided by the background. In the next step, the sample is cleaned by cycles of oxidation with O<sub>2</sub> ( $1 \times 10^{14}$  cm<sup>-2</sup> s<sup>-1</sup>) at 800 K via the effusive source for 10 min and consequent reduction with CO ( $1 \times 10^{14}$  cm<sup>-2</sup> s<sup>-1</sup>) at ~400 K for 5 min. Finally, after the sample is flashed to 600 K and cooled down to the desired temperature, the background is collected on the clean Pt(111) surface and is used in order to calculate the final IR spectrum. During the cleaning procedure, the evolution of O<sub>2</sub>, CO, CO<sub>2</sub>, and the apparent mass is monitored. The oxidation-reduction cycle time can be optimized according to CO<sub>2</sub> desorption from the sample.

To validate the sample cleanliness obtained by the cleaning procedure via molecular beams described above, the IR spectrum of CO was recorded on this surface, which is shown as the lowest curve of Fig. 14(b). Two vibrational bands at 2104 cm<sup>-1</sup> (on-top sites) and at 1854 cm<sup>-1</sup> (bridge sites) were obtained; both the vibrational frequencies and the intensities correspond to that once previously recorded on the clean Pt(111) surface.<sup>34</sup>

Figure 14(a) shows the IRAS spectra of R-NEA on Pt(111) at 155 K at two different coverages. The spectrum obtained at exposure of ~30 L corresponds to a multilayer adsorption of R-NEA and displays distribution of vibrational bands that are characteristic for largely unperturbed molecules similar to the gas phase spectra or condensed phase.<sup>35</sup> The vibration modes at 1512 and 1597 cm<sup>-1</sup> are assigned to in-plane stretching of the naphthyl ring along the long and short axes, respectively. The broad peak at ~1448 cm<sup>-1</sup> is assigned to the asymmetric deformation of the methyl moiety of the ethylamine, and the peak at 1369 cm<sup>-1</sup> is assigned to the symmetric deformation of the methyl. The IR spectra obtained for the submonolayer R-NEA coverages exhibit strong changes in the peak relative intensities which reflects a change in the adsorption geometry. However, the molecular structure of the R-NEA adsorbed from the gas phase seems to be preserved upon adsorption onto the Pt(111). The absence of the peak at 1597 cm<sup>-1</sup> and the relatively small

intensity of the in-plane deformation of the naphthyl ring along the long axis suggest that, at submonolayer coverage, the molecules adopt a tilted geometry of the naphthyl ring with respect to the surface plane and bonding to the Pt surface possibly via the nitrogen atom. At this surface coverage, the tilting is more pronounced along the long axis. The tilted geometry of the naphthalene ring at submonolayer coverages is consistent with IRAS and NEXAFS study previously reported by Zaera and Lambert.<sup>35–37</sup> There is some discrepancy in the assignment of the vibrational bands to the assignment reported in studies by McBreen and co-workers, which need to be addressed in our further studies.<sup>38,39</sup>

In the next step, the adsorption of CO on the Pt surface functionalized with R-NEA was investigated. Figure 14(b) shows the IRAS spectrum of CO adsorbed on R-NEA/Pt(111) at 155 K. The spectrum clearly shows that the peaks of adsorbed CO on the NEA-modified surface are shifted and broadened compared to the pristine surface. The CO adsorbed at the on-top sites is red shifted by 33 cm<sup>-1</sup>, whereas the band related to CO adsorbed at the bridge sites is shifted by 24 cm<sup>-1</sup> as compared to the pristine Pt(111) surface. Additionally, the latter band shows considerable broadening (FWHM = 100 cm<sup>-1</sup>). Both observations point to an intermolecular interaction of CO with the adsorbed R-NEA molecules. Further studies need to be carried out to clarify the origin of these phenomena.

#### IV. CONCLUSIONS

A new compact multimolecular beam/surface spectroscopy experimental setup allowing fundamental-level reactivity studies on ligand-functionalized model (nanostructure) surfaces is introduced. The new apparatus consists of three chambers, which can be operated as independent UHV systems, and a unique combination of tools including two effusive and one supersonic molecular beam, IRAS for the spectroscopic identification of adsorbed surface species, QMS for gas phase analyses, as well as tools required for the preparation and structural characterization of complex nanostructured model catalysts based on the thin oxide films epitaxially grown on

metal single crystals. These tools include LEED/AES, TPD, metal evaporators, as well as calibration methods. Additionally, a dedicated deposition chamber is implemented allowing us to functionalize the catalytic surface with low vapor pressure compounds. The apparatus contains an ambient pressure cell that provides an experimental possibility to carry out the reactivity studies in a broad range of reaction conditions up to the atmospheric pressure.

In this manuscript, we present the constructional details of this setup and its initial performance. Particularly, we show that the new compact design of effusive beams allows for achieving high molecular fluxes typically required in reactivity studies. In the test studies on catalytically relevant materials, adsorption of two different adsorbates—acetophenone and R-NEA—was investigated employing IRAS and molecular beam techniques. We provide a discussion of the observed phenomena.

## ACKNOWLEDGMENTS

The support from the European Research Council (ERC Starting Grant ENREMOS, Project No. 335205) is gratefully acknowledged. The authors gratefully acknowledge the support of Klaus-Peter Vogelgesang (FHI, Department of Physical Chemistry) and Georg Heyne (FHI Elab).

## REFERENCES

- <sup>1</sup>F. Zaera, *Catal. Lett.* **142**(5), 501–516 (2012).
- <sup>2</sup>C. M. Pradier, T. Birchem, Y. Berthier, and G. Cordier, *Catal. Lett.* **29**(3-4), 371–378 (1994).
- <sup>3</sup>P. Gallezot and D. Richard, *Catal. Rev.* **40**(1-2), 81–126 (1998).
- <sup>4</sup>M. E. Chiu, G. Kyriakou, F. J. Williams, D. J. Watson, M. S. Tikhov, and R. M. Lambert, *Chem. Commun.* **2006**, 1283–1285.
- <sup>5</sup>R. A. Sheldon and H. van Bekkum, *Fine Chemicals through Heterogeneous Catalysis* (Wiley-VCH Verlag GmbH, 2007), pp. 351–471.
- <sup>6</sup>S. T. Marshall and J. W. Medlin, *Surf. Sci. Rep.* **66**(5), 173–184 (2011).
- <sup>7</sup>P. Sonstrom and M. Baumer, *Phys. Chem. Chem. Phys.* **13**(43), 19270–19284 (2011).
- <sup>8</sup>A. J. Gellman, W. T. Tysøe, and F. Zaera, *Catal. Lett.* **145**(1), 220–232 (2015).
- <sup>9</sup>S. H. Pang and J. W. Medlin, *J. Phys. Chem. Lett.* **6**(8), 1348–1356 (2015).
- <sup>10</sup>C.-H. Lien and J. W. Medlin, *J. Catal.* **339**, 38–46 (2016).
- <sup>11</sup>F. Meemken and A. Baiker, *Chem. Rev.* **117**(17), 11522–11569 (2017).
- <sup>12</sup>C. W. Jones, K. Tsuji, and M. E. Davis, *Nature* **393**(6680), 52 (1998).
- <sup>13</sup>A. J. McCue, F.-M. McKenna, and J. A. Anderson, *Catal. Sci. Technol.* **5**(4), 2449–2459 (2015).
- <sup>14</sup>K. Y. Lee, Y. W. Lee, J.-H. Lee, and S. W. Han, *Colloids Surf., A* **372**(1-3), 146–150 (2010).
- <sup>15</sup>D. J. Snelders, N. Yan, W. Gan, G. Laurenczy, and P. J. Dyson, *ACS Catal.* **2**(2), 201–207 (2012).
- <sup>16</sup>S. T. Marshall, M. O'Brien, B. Oetter, A. Corpuz, R. M. Richards, D. K. Schwartz, and J. W. Medlin, *Nat. Mater.* **9**(10), 853–858 (2010).
- <sup>17</sup>L. Rodríguez-García, K. Hungerbühler, A. Baiker, and F. Meemken, *ACS Catal.* **7**(6), 3799–3809 (2017).
- <sup>18</sup>T. Mallat, E. Orglmeister, and A. Baiker, *Chem. Rev.* **107**(11), 4863–4890 (2007).
- <sup>19</sup>K.-H. Dostert, C. P. O'Brien, F. Mirabella, F. Ivars-Barceló, S. Attia, E. Spadafora, S. Schauermaun, and H.-J. Freund, *ACS Catal.* **7**, 5523–5533 (2017).
- <sup>20</sup>C. P. O'Brien, K.-H. Dostert, S. Schauermaun, and H.-J. Freund, *Chem.–Eur. J.* **22**(44), 15856–15863 (2016).
- <sup>21</sup>C. P. O'Brien, K. H. Dostert, M. Hollerer, C. Stiehler, F. Calaza, S. Schauermaun, S. Shaikhutdinov, M. Sterrer, and H.-J. Freund, *Faraday Discuss.* **188**, 309–321 (2016).
- <sup>22</sup>K.-H. Dostert, C. P. O'Brien, F. Ivars-Barceló, S. Schauermaun, and H.-J. Freund, *J. Am. Chem. Soc.* **137**(42), 13496–13502 (2015).
- <sup>23</sup>J. Libuda and H.-J. Freund, *Surf. Sci. Rep.* **57**(7-8), 157–298 (2005).
- <sup>24</sup>W. Ludwig, A. Savara, S. Schauermaun, and H.-J. Freund, *ChemPhysChem* **11**(11), 2319–2322 (2010).
- <sup>25</sup>F. M. Hoffmann, *Surf. Sci. Rep.* **3**(2-3), 107–192 (1983).
- <sup>26</sup>H.-J. Freund, M. Bäumer, J. Libuda, T. Risse, G. Rupprechter, and S. Shaikhutdinov, *J. Catal.* **216**(1-2), 223–235 (2003).
- <sup>27</sup>J. Libuda, I. Meusel, J. Hartmann, and H.-J. Freund, *Rev. Sci. Instrum.* **71**(12), 4395–4408 (2000).
- <sup>28</sup>T. Reisinger, G. Bracco, S. Rehbein, G. Schmahl, W. E. Ernst, and B. J. Holst, *J. Phys. Chem. A* **111**(49), 12620–12628 (2007).
- <sup>29</sup>*Atomic and Molecular Beam Methods*, edited by G. Scoles (Oxford University Press, New York, Oxford, 1988), Vol. 1, p. 254.
- <sup>30</sup>G. Rupprechter, *Adv. Catal.* **51**, 133–263 (2007).
- <sup>31</sup>G. Rupprechter, H. Unterhalt, M. Morkel, P. Galletto, L. Hu, and H.-J. Freund, *Surf. Sci.* **502**, 109–122 (2002).
- <sup>32</sup>S. Stein, W. Mallard, and P. Linstrom, *NIST Chemistry WebBook*, NIST Standard Reference Database Number Vol. 69 (National Institute of Standards and Technology, 2003).
- <sup>33</sup>A. Gambi, S. Giorgianni, A. Passerini, R. Visinoni, and S. J. Ghersesti, *Spectrochim. Acta, Part A* **36**(10), 871–878 (1980).
- <sup>34</sup>H. Steininger, S. Lehwald, and H. Ibach, *Surf. Sci.* **123**(2-3), 264–282 (1982).
- <sup>35</sup>Y. Ni, A. D. Gordon, F. Tanicala, and F. Zaera, *Angew. Chem., Int. Ed.* **129**(27), 8071–8074 (2017).
- <sup>36</sup>J. M. Bonello, F. J. Williams, and R. M. Lambert, *J. Am. Chem. Soc.* **125**(9), 2723–2729 (2003).
- <sup>37</sup>I. Lee, Z. Ma, S. Kaneko, and F. Zaera, *J. Am. Chem. Soc.* **130**(44), 14597–14604 (2008).
- <sup>38</sup>V. Demers-Carpentier, G. Goubert, F. Masini, R. Lafleur-Lambert, Y. Dong, S. Lavoie, G. Mahieu, J. Boukouvalas, H. Gao, and A. H. Rasmussen, *Science* **334**(6057), 776–780 (2011).
- <sup>39</sup>Y. Zeng, F. Masini, A. H. Rasmussen, M. N. Groves, V. Albert, J. Boukouvalas, and P. McBreen, *Surf. Sci.* **676**, 17–22 (2018).